Proceedings of the ASME 2020
International Mechanical Engineering Congress and Exposition
IMECE2020
November 15-18, 2020, Portland, OR, USA

IMECE2020-24311

ENHANCED WICKABILITY OF THIN NON-UNIFORM SINTERED PARTICLE WICKS USING LATTICE BOLTZMANN METHOD

Mohammad Borumand[1], Taehun Lee[2], and Gisuk Hwang[1]

[1]Department of Mechanical Engineering, Wichita State University, Wichita, KS, 67260
[2] Department of Mechanical Engineering, The City College of New York, New York City, NY, 10031

ABSTRACT

Thin non-uniform particle size wicks are essential to improve the maximum heat flux of two-phase thermal management systems by improving the wickability. To understand the enhanced wickability, we examine a pore-scale capillary flow within the thin sintered particle wick using a free-energy-based, single-component, two-phase Lattice Boltzmann Method (LBM) with a minimal parasitic current. The developed LBM approach is validated through the rate-of-rise in the two-parallel plates with parallel plates spacing of W=48 against analytical Bosanquet equation, achieving the RMS error below 10%. The LBM predicts the rate-of-rise through the uniform and non-uniform particle-size wicks between two-parallel plate, including the capillary meniscus front and dynamic capillary filling. At the same plate spacing and porosity, i.e., W = 48 lu and ε = 0.75, the non-uniform particle size wick achieves enhanced wickability by providing the selective flow pathway through pore networks formed in the smaller pores between the small/large particles, which is in qualitative agreement with previous experimental results. The enhancement of the maximum and minimum dimensionless liquid height and the liquid-filled pore ratio of non-uniform particle size wick is found to be up to 11.1, 27.47, and 26.11%, respectively. The simulation results provide insights into the optimal wick structures for high heat flux two-phase thermal management system by enhancing the wickability through the non-uniform particle (or pore) sizes.

Keywords: rate of rise, permeability, optimal wick structure, capillary flow

NOMENCLATURE

a	constant
b	constant
c_s	speed of sound, lu/ts
D_p	average particle size, lu
E_0	bulk energy, mu-lu^2/ts^2
$\mathbf{e}$	microscopic particle velocity, lu/ts
$\mathbf{F}$	intermolecular interaction force, mu-lu/ts^2
f_α	distribution function
f_α^{eq}	equilibrium distribution function
g	gravitational acceleration, lu/ts^2
h	liquid height, lu
h_0	submersion length of the plates, lu
h_1	initial liquid surface-particle gap, lu
h^*	dimensionless liquid height
K	permeability, lu^2
Lp	large pore, lu
r_c	meniscus radius, lu
r_p	particle radius, lu
Sp	small pore, lu
p	pressure, mu/lu-ts^2
t	time, ts
t^*	dimensionless time
$\mathbf{u}$, $\mathbf{U}$	macroscopic velocity, lu/ts
W	plate spacing, lu

Greek symbols

ρ	density, mu/lu^3
σ	surface tension, mu/ ts^2
δx	x-direction lattice spacing, lu
δy	y-direction lattice spacing, lu
δt	time spacing, ts
λ	relaxation time, ts
μ	chemical potential, lu^2/ts^2
κ	gradient parameter, mu^3/lu^5
β	constant
θ_{eq}	equilibrium contact angle
θ_d	dynamic contact angle
ε	porosity of the particle bed
η	liquid-filled pore ratio or liquid saturation
Ω	dimensionless wetting potential
α	angle related to equilibrium contact angle
ϕ	constant related to density on solid surface
ψ	mixing energy density, mu-lu^2/ts^2

subscripts

c	capillary
eq	equilibrium
l	liquid phase
p	particle
s	solid wall or surface
sat	saturation
v	vapor phase

1. INTRODUCTION

The ever-growing heat flux associated with modern miniaturized and compact electronic and power conversion systems requires advanced thermal control systems with high heat flux thermal management capabilities. Employing the large latent heat of evaporation of the working fluid, i.e., two-phase cooling systems, such as heat pipes and vapor chamber, provide an efficient and reliable thermal management compared to single phase cooling mechanisms, i.e., forced convection over the extended surfaces. However, the maximum heat transfer capability of the heat pipes is limited by poor coolant supply to the heating surface through capillary flow which in turn results in premature surface dryout and eventual operation failure.

Thin evaporating wicks combined with thick liquid artery wicks have significantly improved maximum heat flux and reduced thermal resistance across the wicks [1,2], and they can be further improved by utilizing thin wicks with non-uniform particle size distribution, i.e., bimodal wick [3,4]. The enhanced two-phase cooling capability is attributed to the improved capillary flow from the selective liquid percolation through smaller pores associated with the non-uniformity in particle size, but the additional efforts are critically needed to further understand the pore-scale capillary flow enhancement mechanisms as the current capillary flow understanding primarily remains in the thick uniform particle size wick. Holley and Faghri [5] have measured the rate-of-rise and effective pore radius of the thin porous media, while the permeability has been estimated by curve-fitting the rate-of-rise into the developed force balance equation.

Over the past few decades, Lattice Boltzmann method (LBM) has emerged as a powerful tool for simulation of flow in complex geometries such as porous media. The main benefit of the LBM is the simple boundary condition implementations, especially for the non-uniform pore distribution over other alternatives such as Volume of Fluid (VOF). The implementation of complicated solid boundaries can be achieved conveniently through bounce-back rule. The previous LBM approaches have been used to study fluid flows in porous media, but those mainly focus on single phase flow [6] and capillary flow in fibrous porous materials [7]. Hoef et al. [6] developed a single-phase LBM to model low-Reynolds-number gas flow over mono- and bi-disperse arrays of spheres and reported results for permeability and drag force. Nabovati et al. simulated [7] fluid flow in three-dimensional random fibrous media using single-phase model, and reported the permeability of the medium using the Darcy law across a wide range of void fractions. Recently, Liu et al. [8] has examined two-phase fluid flow of gas displacing liquid in particle-bed porous media, mainly focusing on uniform particle sizes. In this study, the thin particle size wick is examined using the two-phase free-energy-based LBM approach, especially for understanding the enhanced capillary flow mechanisms through non-uniform particle size distribution.

This paper is organized as follows. In Section 2, the working principles of enhanced capillary flow in uniform and non-uniform wicks are discussed. In Section 3, the mathematical formulation of the LBM is presented, including the illustration of the LBM simulation details and validation. In Section 4, the predicted rate-of-rise in the uniform and nonuniform particles in the two-parallel plates are shown, including discussions. Finally, a conclusion will be made.

2. WORKING PRINCIPLES

An ideal wick structure for the two-phase cooling systems requires not only a large capillary pressure, i.e., capillary pumping capability, but also a large permeability for maximum liquid coolant supply to the heated surface. The maximum capillary pressure, p_c, is inversely proportional to the capillary meniscus radius given as [9]

$$p_c = \frac{2\sigma}{r_c} \tag{1}$$

where σ is the surface tension, and r_c is the capillary meniscus radius, while the permeability K is given as [9]

$$K = a\frac{\varepsilon^3 {r_p}^2}{(1-\varepsilon)^2} \tag{2}$$

where ε is the porosity, a is a constant, and r_p is the particle radius. Note that the capillary meniscus radius, r_c is proportion to the particle radius, r_p [9]. In the wick structure with the uniform particle size, to increase the capillary pressure, one can use the small particle size to increase the capillary pressure by $1/r_p$. However, the small particle size also decreases the permeability by ${r_p}^2$, which in turn results in the overall wickability reduction. To simultaneously increase the capillary pressure and permeability, the non-uniform particle sizes can be used, while the small particle size can increase the capillary pressure and the large particle leads to the large permeability [3,10] as shown in Figure 1.

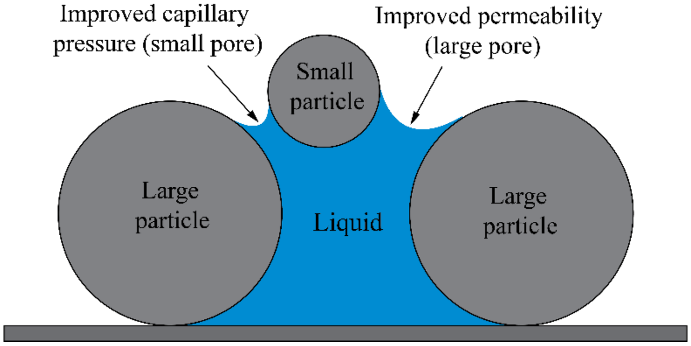

Figure 1: Schematic of the liquid-filled sintered particle wick with nonuniform particle size distribution. Non-uniform capillary meniscus radii are also shown.

Recent experimental studies show that the wicks with nonuniform particle sizes enhance the heat flux and heat transfer coefficient by improving capillary flow and permeability as well as creating additional evaporation sites [4]. In this study, the pore-scale enhanced wicking mechanisms of the non-uniform particle sizes are examined using the LBM as described below.

3. LATTICE BOLTZMANN METHOD (LBM)

3.1 Governing Equations and Boundary Conditions

To simulate the pore-scale capillary flow in the sintered particle wicks, the LBM is used. The discrete Boltzmann equation (DBE) for the van der Waals fluid with Bhatnagar-Gross-Krook (BGK) collision operator can be written as [11]

$$\frac{\partial f_\alpha}{\partial t} + \mathbf{e}_\alpha \cdot \nabla f_\alpha = -\frac{f_\alpha - f_\alpha^{eq}}{\lambda} + \frac{(\mathbf{e}_\alpha - \mathbf{u}) \cdot \mathbf{F}}{\rho c_s^2} f_\alpha^{eq} \qquad (3)$$

where f_α is the particle distribution function, $\mathbf{e}_\alpha$ is the microscopic particle velocity, $\mathbf{u}$ is the macroscopic velocity, ρ is the density, c_s is the speed of sound, λ is the relaxation time, f^{eq} is the equilibrium distribution function, and $\mathbf{F}$ is the averaged external force experienced by each particle, i.e., intermolecular interaction force. Note that $c_s = c/\sqrt{3}$, where $c = \delta x/\delta t$ is the lattice speed, and δx, δy, and δt are 1 respectively. Diffuse interface methods like LBM generally suffer from the existence of spurious currents. These undesirable currents are small-amplitude velocity fields that arise from imbalance between discretized forcing terms at the phase interface. Recently, Lee and Fischer [12] utilized the phase field theory to develop a new forcing scheme in Lattice Boltzmann Equation (LBE) in which the spurious currents are eliminated to round-off. This forcing scheme, so called the potential form, can be expressed as given as

$$\mathbf{F} = \nabla(\rho c_s^2) - \rho \nabla(\mu_0 - \kappa \nabla^2 \rho) \qquad (4)$$

where κ is the gradient parameter and μ_0 is the chemical potential. The equilibrium properties of an isothermal thermodynamic system that contains wall boundaries can be described by summing the bulk free energy and a linear wall free energy [13]. Therefore, the total free energy will take the following form

$$\Psi_b + \Psi_s = \int_\Omega \left(E_0(\rho) + \frac{\kappa}{2}|\nabla\rho|^2\right) d\Omega - \int_\Gamma \varphi_1 \rho_s \, d\Gamma \qquad (5)$$

In the vicinity of the critical point, the equation of state can be simplified, thereby resulting in the following approximation for the bulk energy E_0

$$E_0(\rho) = \beta(\rho - \rho_v^{sat})^2(\rho - \rho_l^{sat})^2 \qquad (6)$$

where ρ_l^{sat} and ρ_v^{sat} are the liquid and vapor densities at saturation, respectively, and β is the constant related to the compressibility of the bulk phase. The chemical potential μ_0 is related to the bulk energy given as

$$\mu_0 = \frac{\partial E_0}{\partial \rho} \qquad (7)$$

The gradient parameter κ and the liquid-vapor surface tension force σ are

$$\kappa = \frac{\beta D^2 (\rho_l^{sat} - \rho_v^{sat})^2}{8} \qquad (8)$$

$$\sigma = \frac{(\rho_l^{sat} - \rho_v^{sat})^3}{6} \sqrt{2\kappa\beta} \qquad (9)$$

where D is the interface thickness which should be greater than 3 lattice units for numerical stability. Here, we used $D = 4$. The relation between φ_1 in Eq.(5), the dimensionless wetting potential Ω, and the equilibrium contact angle θ_{eq} can be expressed by

$$\Omega = \frac{4\varphi_1}{(\rho_l^{sat} - \rho_v^{sat})^2} \sqrt{2\kappa\beta} \qquad (10)$$

$$\Omega = 2\,\mathrm{sgn}\left(\frac{\pi}{2} - \theta_{eq}\right)\left(\cos\left(\frac{\alpha}{3}\right)\left[1 - \cos\left(\frac{\alpha}{3}\right)\right]\right)^{\frac{1}{2}} \qquad (11)$$

where

$$\alpha = \arccos(\sin\theta_{eq})^2 \,. \qquad (12)$$

It follows that the boundary condition at the wall for $\nabla^2\rho$ in Eq.(4) would take the form of

$$\kappa \mathbf{n} \cdot \rho_s = -\phi_1 \qquad (13)$$

where $\mathbf{n}$ is the unit vector normal to the wall. By establishing the appropriate boundary condition for Laplacian using Eq.(13), $\mu = \mu_0 - \kappa\nabla^2\rho$ can be treated as a scalar, which avoids the development of parasitic currents at the phase interface. The values of the LBM parameters used in the present study are summarized in Table 1. All values are in lattice unit, i.e., a combination of lattice length unit (lu) and lattice time unit (ts).

Table 1. Values of the parameters used in the LBM simulations

LBM Parameter	Magnitude in Lattice Unit
δx	1
δx	1
δt	1
ρ_l^{sat}	1
ρ_v^{sat}	0.2
θ_{eq}	30°
c_s	$1/\sqrt{3}$
g	0
λ	0.5
σ	1.365×10^{-3}
β	0.01
κ	0.0128
D	4
h_0	93
h_1	2
h_2	161

The unknown particle distribution at the wall can be found by implementing equilibrium boundary condition, which essentially includes the calculation based on the bounce back rule after streaming, followed by the immediate relaxation toward the equilibrium state. This condition implies that any unknown variable ϕ near the wall should be approximated by

$$\phi(\mathbf{x}_s + \mathbf{e}_\alpha \delta t) = \phi(\mathbf{x}_s - \mathbf{e}_\alpha \delta t)$$
$$\phi(\mathbf{x}_s + 2\mathbf{e}_\alpha \delta t) = \phi(\mathbf{x}_s - 2\mathbf{e}_\alpha \delta t) \qquad (14)$$

where $\mathbf{x}_s$ is the wall node and δt is the time step. ρ and μ at the wall boundary should be calculated using Eq. (14). Further details on the wall boundary conditions are found in the previous work [13]. Since a normal vector cannot be defined at the sharp corners of solid particles and plates, special boundary treatment is necessary. Here, we have used the isotropic method proposed by Connington et al. [14]

To validate the LBM, the rate-of-rise between the two plates using the LBM are compared with the closed-form solution, so called Bosanquet equation, given as [15]

$$(h^* + h_0^*)\frac{d^2h^*}{dt^{*2}} + (\frac{dh^*}{dt^*})^2 + (h^* + h_0^*)\frac{dh^*}{dt^*} = a\cos\theta_d - bh^* \qquad (15)$$

where $h^*=h(t)/W$ and $h_0^*=h_0/W$ are dimensionless liquid height above the liquid-vapor surface and dimensionless liquid-submerged length, respectively, as shown in Figure 2. The W is the space between two parallel plates, $t^*=t/t_0$ is the dimensionless time and $t_0 = \rho_l (W^2)/12\mu_l$, $a = 2\rho_l (W) \sigma/(12\mu_l)^2$ and $b = \rho_l^2 (W)^3 g/(12\mu_l)^2$, g and σ are gravitational acceleration and surface tension, respectively. We have also decided to work with static contact angle for the sake of simplicity. The simplified Bosanquet equation was solved using 4th order Runge-Kutta method. Figure 3 shows a comparison between the LBM simulation results and the solutions of Eq.(15) for W =48 and g=0, which agree well. Note that the liquid height, h^* in the LBM predicts the maximum (capillary meniscus liquid front near the plate) and the minimum heights (central part of the capillary meniscus recess), and only minimum height is shown in Figure 3, showing the RMS error below 10%. A detailed analysis of the capillary rise between parallel plates under dynamic conditions and by considering the effect of long-range interactions between the fluid and solid walls is presented in the previous work [15].

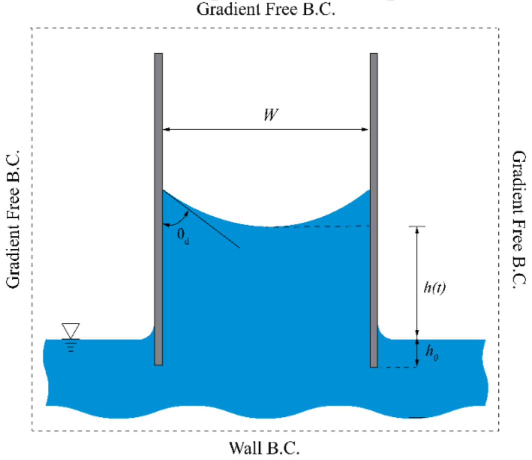

Figure 2: Rate of rise between two parallel plates in contact with a liquid reservoir. The space between the plates, W, the liquid height, h, the liquid-submerged depth, h_0, and static contact angle θ_d, and the boundary conditions are also shown.

3.2 LBM Simulations

To investigate the effects of nonuniform particle size distribution on enhanced wickability, uniform and nonuniform simulations are performed as shown in Figure 4. In Figure 4(a), the two parallel plates are filled with uniform square particles (case 1), while Figure 4(b) and (c) show non-uniform square particles between the two plates with the spacing of W (case 2 and 3, respectively). In case 3, the small pores (Sp6 and Sp8) are smaller than the corresponding pores in case 2 resulting in higher capillary pumping capability. In addition, the larger pores in case 3 (Lp3 and Lp4) are larger than the corresponding pores in case 2, offering large liquid-permeable space. These have been achieved by moving the smaller particles closer to the larger particle and/or closer to the wall.

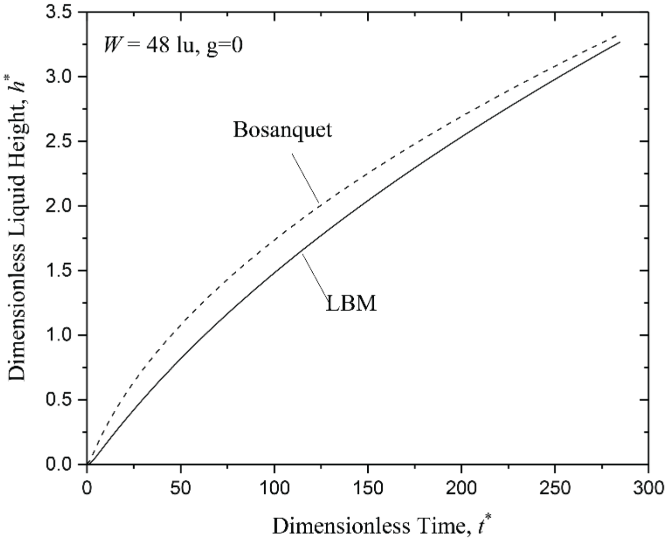

Figure 3: Predicted LBM results for the rate of rise between parallel plates with W = 48 lu and g = 0, compared with close-form solution, i.e., the Bosanquet equation, Eq.(15).

Note that all three cases have the same number of particles (4 rows and 3 columns of particles) with the same porosity, ε = 0.75. Except for the wall boundary at the bottom, the rest of the boundary conditions are gradient free. Table 2 and 3 summarize the dimensions of the distance between the plates and uniform/non-uniform pores used in the LBM simulations shown in Figure 4.

The liquid-vapor density ratio, spacing of the parallel plates and the porosity of the medium are $\rho_l/\rho_v = 5$, $W = 48$ lu, respectively. The LBM simulation size is a 721×251 lattice, where the liquid-vapor interface outside the parallel plates does not change significantly due to the loss of liquid by capillary flow. The initial liquid elevation above the bottom boundary h_2, the liquid submerged length h_0 and the gap between the initial liquid-vapor interface, and the first row of particles h_1 are 161, 93 and 2 lu, respectively. The contact angle is 30° inside the parallel plates, while it is 90° at the outside of the plates to prevent the liquid from climbing up at the external side of the wall.

Table 2: Summary of the LBM simulation dimensions for uniform particle size distribution setup.

Simulation parameter	Magnitude, Lattice Unit (Case 1)
W	48
$l_{x1}, l_{x2}, l_{x3}, l_{x5}$	8
l_{x4}	4

Table 3: Summary of the LBM simulation dimensions for nonuniform particle size distribution for two different setups.

Simulation parameter	Magnitude, Lattice Unit (Case 2)	Magnitude, Lattice Unit (Case 3)
W	48	48
l_{x1}, l_{x2}	4	4
l_{x3}, l_{x4}	10	10
l_{x5}	8	8
l_{x6}, l_{x12}	4	4
l_{x7}	5	5
l_{x8}	3	0
l_{x9}	10	11
l_{x10}	5	4
l_{x11}	3	6

Note that the contact angle of the external wall does not influence the fluid flow inside of the two plates. Furthermore, since this study focuses on the capillary-driven flow, i.e., low Bond number we have neglected the effect of gravity by choosing $g = 0$ lu/ts^2.

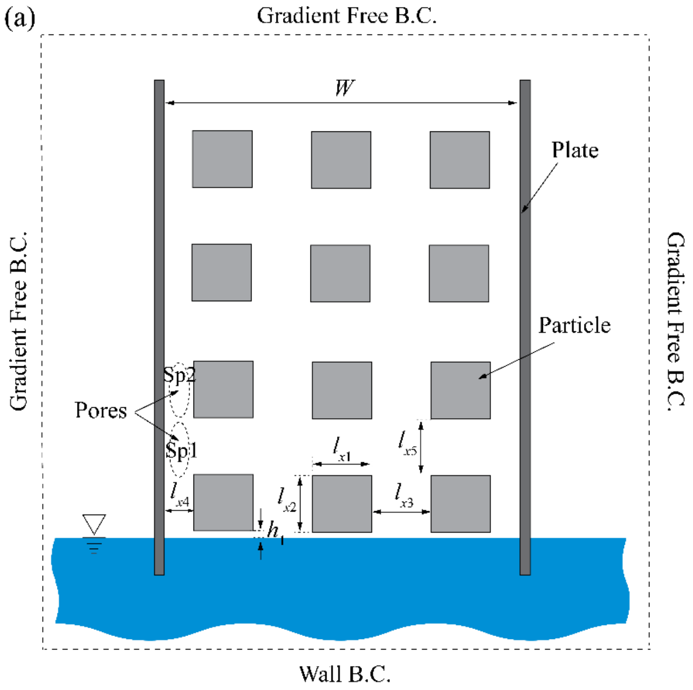

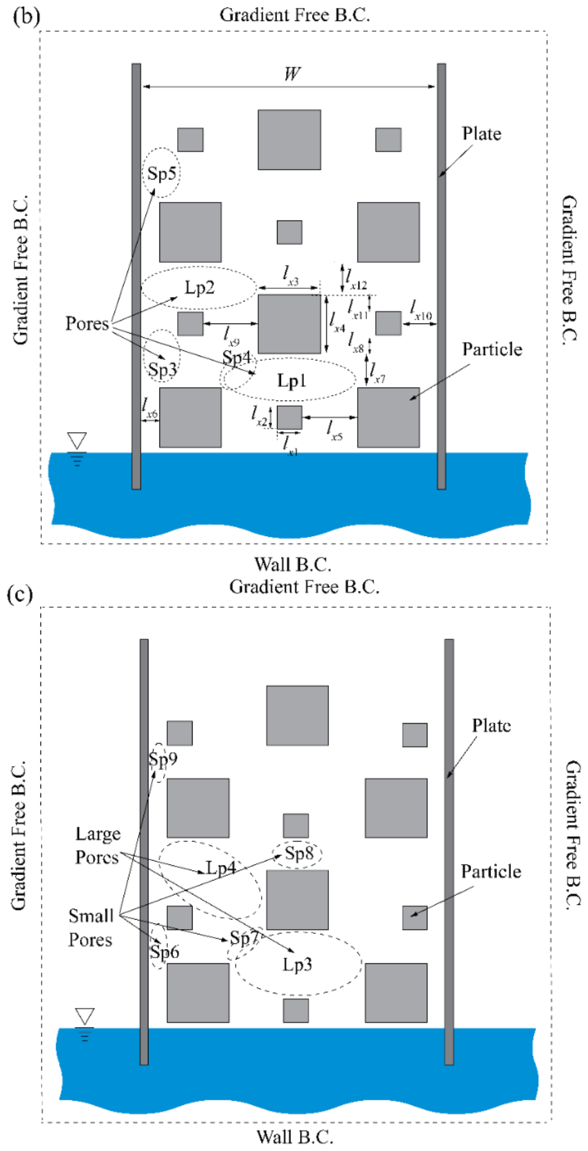

Figure 4: (a) Uniform particle-filled two parallel plates (case 1), (b) nonuniform particle-filled two parallel plates (case 2), and (c) modified nonuniform particle-filled two parallel plates showing the small pores (Sp) and large pores (Lp) created (case 3). The plates, particles, pore sizes and boundary conditions are also shown.

4. RESULTS AND DISCUSSION

In this section, the LBM simulation predicts the rate-of-rise through uniform/non-uniform particle wick, especially for the enhanced wickability of the non-uniform particle wick along with discussions. Figure 5(a) shows the maximum dimensionless liquid height of the capillary meniscus front, h^*, as a function of dimensionless time, t^*. As the time increases, the maximum liquid height increases for all three cases, with different rate-of-rise at given time. In other words, initially it sharply increases, then it slows down for a certain period of time until it sharply increases again, i.e., periodic sharp rate of rise.

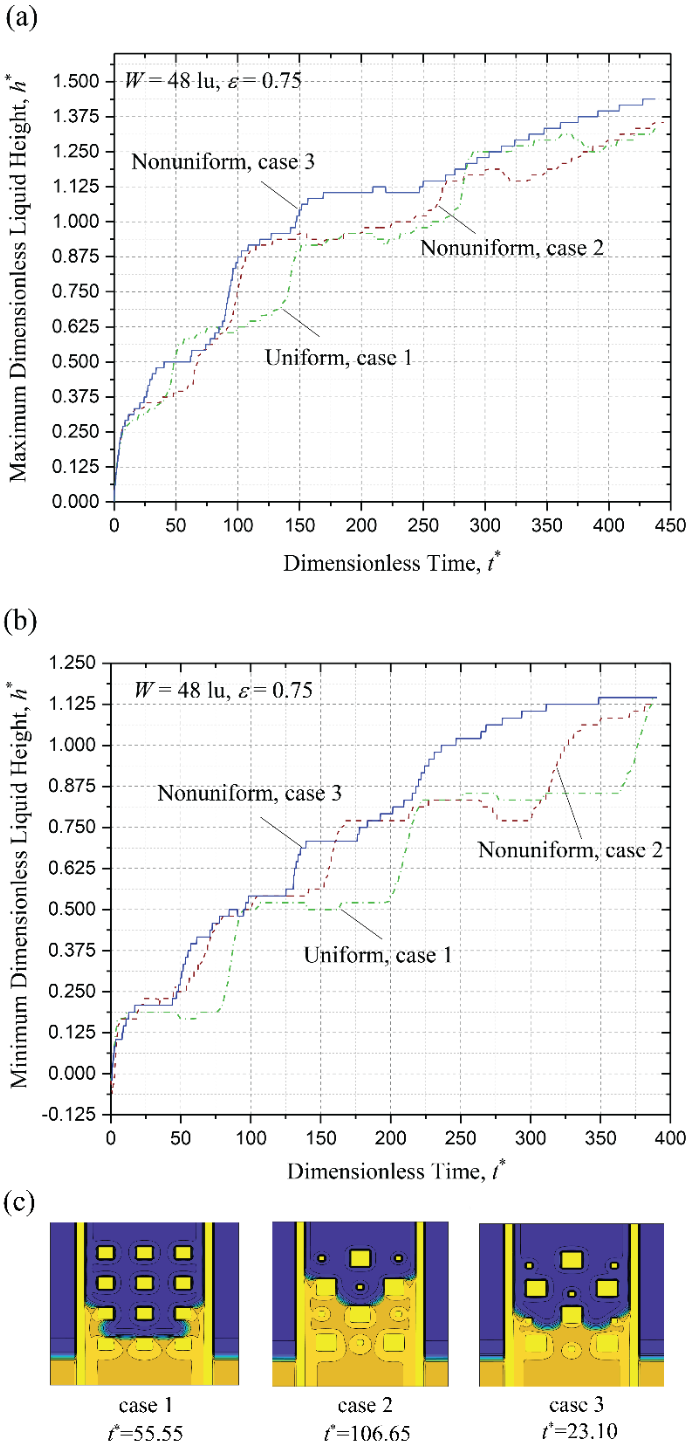

case 1
t^*=55.55

case 2
t^*=106.65

case 3
t^*=23.10

Figure 5: (a) Maximum and (b) minimum dimensionless liquid height as a function of dimensionless time, t^*, and (c) snapshots of rate of rise simulation at different time steps for uniform (case 1) and nonuniform (case 2 and 3) particle size distribution. The plate spacing W and porosity, ε, are also shown.

The sharp rate-of-rise periods are mainly associated with the rise of liquid in the small pores between the particles (adjacent to the plates) and the plates, while the slow ones between the sharp ones, i.e., plateaus, correspond to the delayed capillary flow to the upper particles. In uniform particle wick (case 1), the plateau periods are larger than the other cases, and the three periods increase as the time increases, indicating that the period of maintaining the plateaus increases as the liquid height increases. The duration of the first plateau is inversely proportional to the pore size formed between the first and second rows of particles adjacent to the plates [Sp1 in Figure 4(a), Sp3 in (b) and Sp6 in (c)], i.e., the smaller the pore size, the higher the capillary pressure which in turn results in a faster rate of rise and hence a shorter plateau in liquid height. The marginally higher rate of rise for case 1 at t^* = 55.55 is related to the rapid capillary rate-of-rise through the small but lengthy pore between the particle and plate in the second particle row, i.e., Sp2 in Figure 4(a), as shown in Figure 5(c). However, this sharp rise is followed by a relatively large plateau period, i.e., second plateau of case 1 in Figure 5(a) from t^* = 50 to t^* = 130 because it needs some time for the liquid to fully fill the pores between the first and second particle rows. On the other hand, the second plateaus for case 2 and 3 are relatively short, and the liquid can rise quickly through the pores in the second particle row until it reaches the top surface of the large particles at the third row. Figure 5(c) shows the corresponding snapshot for case 2 at t^* = 106.65. This sharp rate of rise is in part due to the combination of small and large pores between the particles in the in the first and second rows, i.e., Lp1 and Sp4 in Figure 4(b), and Lp3 and Sp7 in (c). While the large pores provide enough space for liquid flow, the small pores create a high capillary pressure which improves the liquid rise from one particle layer to the next. Figure 5(c), case 3, illustrates how the liquid flows through the small pores in diagonal direction, i.e., Sp4 and Sp6, which is much different from the case 1. Furthermore, the large permeable pores in the second particle row, i.e., Lp2 and Lp4 in Figure 4(b) and (c), respectively, improve the permeability of the nonuniform particle size wick. The sharp rate-of-rise of the non-uniform particle size wicks (cases 2 and 3) occurs at 50 < t^* < 70, which is followed by a long plateau. The rapid capillary front advancement is shown in Figure 5(c), case 2. This is due to the fact that the pore between the plate and the particles at the third and fourth particle rows, i.e., Sp5 in Figure 4(b), is not small enough to create the necessary capillary pressure for the rise of capillary meniscus front and hence the liquid should fill the remaining pores in the third particle row until it can rise to the next particle row. On the other hand, the small pore at the same location for case 3, i.e., Sp9, assists the liquid rise by providing a large capillary pressure which results in a smaller plateau, i.e., sharp rate of rise at t^* = 145. In Figure 5(a), the instantaneous enhancement of the maximum dimensionless heights of the capillary front of the non-uniform particle size wick (case 2) is 43.5% compared to that of the uniform particle size wick (case 1) at t^* = 105, while it is about 45% in the non-uniform particle size wick (case 3) at t^* = 105. The cumulative (time integral) enhancement of the maximum dimensionless heights of the capillary front of the non-uniform particle size wick (case 2) is 1.24% compared to that of the uniform particle size wick (case

1), while it is 11.1% in the non-uniform particle size wick (case 3).

Figure 5(b) shows the minimum liquid height of the capillary flow, i.e., bottom portion of the capillary meniscus. Similarly observed in the maximum height, the minimum height also shows the periodic sharp rate-of-rise, but the plateaus are completely flat, i.e., no minimum height change for a certain period time. This is associated with the delayed capillary meniscus crescent detachment from the top corners of the particles. The non-uniform particle wicks, especially case 3, show shorter plateau periods, since the liquid quickly fills the small pores (along the diagonal direction) between the particles in different rows [such as Sp4 in Figure 4(b), and Sp7 in (c), respectively]. The detailed explanations on the delayed capillary meniscus crescent detachment are found in previous work [16]. The instantaneous enhancements of the minimum dimensionless heights of the capillary front of both of the non-uniform particle size wicks (case 2 and 3) are around 160% compared to that of the uniform particle size wick (case 1) at $t^* = 79$. The cumulative (time integral) enhancement of the minimum dimensionless heights of the capillary front of the non-uniform particle size wick (case 2) is 13.43% compared to that of the uniform particle size wick (case 1), while it is 27.47% in the non-uniform particle size wick (case 3).

Figure 6 illustrates the snapshots of the rate-of-rise for uniform particle size wick at different simulation time steps. Figure 6(a) shows the initial liquid height within the two plates, which stays in the same level of the liquid pool at $t^* = 0$. (b) In the early stage of the simulation, i.e., $t^* = 0.4$, the liquid quickly interacts with the inner wall and bottom surface of the particle in the first row due to the attractive intermolecular forces between the liquid and solid surfaces. Note that at the very early stages, i.e., $t^* < 0.4$, the minimum liquid height, i.e., central part of the liquid, is lower than the liquid height in the pool due to the capillary meniscus formation as observed in Figure 5(b). (c) As the time increases, at $t^* = 5.21$, the liquid rises quickly to the top surface of the first particle layer. Once the liquid height reaches the same height of the top surface of the first particle row at $t^* = 5.21$, the liquid level stays nearly the same until the liquid rises along the side wall toward the second particle layer. (d) Once liquid reaches the particle at the second row, i.e., $t^* = 41.23$, it rises quickly to the top surface of the particle by the capillary flow through the pores between the wall and the particles adjacent to the wall [Sp2 in Figure 4(a)], i.e., the small capillary meniscus radius in the small pores. This is shown in (e), i.e., $t^* = 55.55$. (f) The liquid in the central part of the capillary meniscus stays at the same level of the top surface of the first particle row, i.e., $t^* = 63.80$, until it finally detaches from the top surface of the first particle row. As previously mentioned in this section, this delayed liquid rise due to the corner of the particle has been similarly observed in the previous work [16], which studied on the interaction of fluid interfaces with immersed solid particles. (g) Once the liquid detaches from the top surface of the particle, $t^* = 80.73$, (h) the liquid-vapor interface very quickly rises toward the upper layer until it touches the bottom surface of the second particle row at $t^* = 84.63$.(i) The liquid then rises quickly through the pores between the particles. (j) The liquid finally rises to the top surface of the second particle layer. In a sense, (j) and (c) are similar, which means that after the step (j), the liquid repeats the similar wetting and capillary flow behaviors observed in (c)-(j).

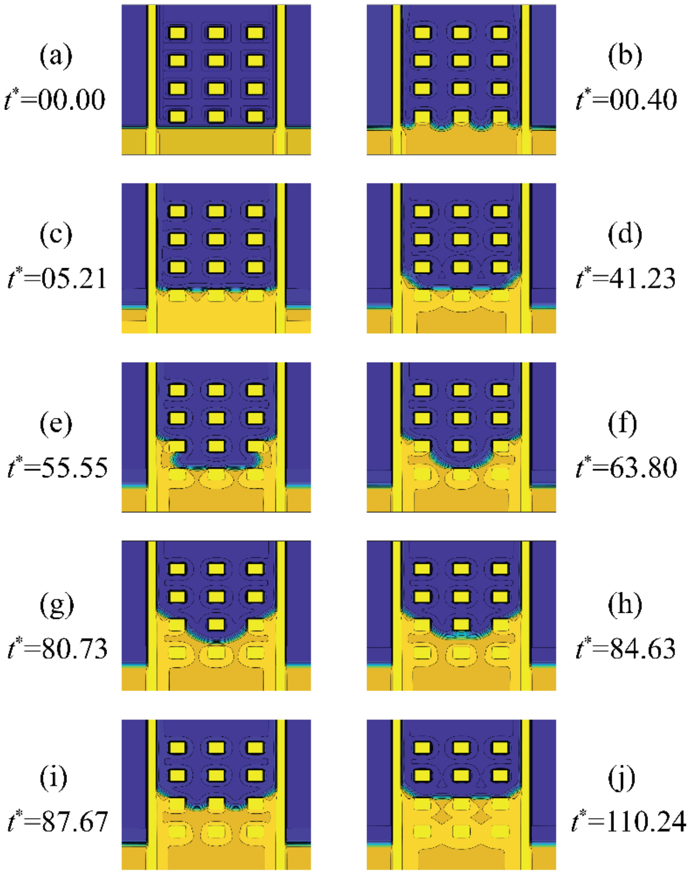

Figure 6: Snapshots of rate of rise in particle-filled parallel plates with uniform particle size wick (case 1). The dimensionless time, t^*, corresponding to each of the snapshots are also shown.

Figure 7 illustrates the snapshots of the rate-of-rise for nonuniform particle size wick case 2 at different simulation time. Figure 7(a) shows the final stage of the first sharp rate of rise at $t^* = 7.81$, after which the liquid level remains nearly the same for a long period (first plateau). (b) Unlike case 1 in which liquid rises from first particle row to the second during the first plateau only due to interaction with the wall, in case 2 the small pore in the diagonal direction between the large particles in the first and second layer, i.e., Sp4 in Figure 4(b), provides a high capillary pressure which assist liquid rise between first and second particle rows, i.e., $t^* = 36.37$. (c) The capillary meniscus crescent finally detaches from the top surface of the large particle at first row, i,e., $t^* = 55.99$, and it rises through the pore between the middle large particle at second particle row and plate at a moderate rate. (d) The liquid reaches the small particles at the second particle row at $t^* = 71.27$. (e) since the pore between the particle and plate is smaller than the pore between the particles at the second particle row, the associated higher capillary pressure adjacent to the plate provides a faster rate of rise until the meniscus reaches the particle at the third row, i.e., $t^* = 98.90$. (f) The liquid experiences a sharp rate of rise in the small pore between the particle and the plate in the third particle row, i.e. $t^* = 106.6$. (g) It takes a long time for the meniscus to detach from the top surface of the large middle particle at the third particle row due to both the corner effect and the relatively large surface length of the large particle. The meniscus finally detaches at $t^* = 155.2$ while the liquid is rising adjacent to the plate. (h) Liquid rises through the pores between the particles. The liquid level adjacent to the wall does not change significantly, though. (i) After a very long time the capillary meniscus adjacent to the plate reaches the small particle at the fourth particle row at $t^* = 264.1$. (j) The liquid rises quickly through the small pore between the particle and plate. This rise requires the meniscus at the center to recede as observed by comparing the capillary meniscus front of (i) and (j) at the center of the parallel plates. This observation can explain the sudden decrease in minimum liquid height at $264 < t^* < 280$ in Figure 5(b). The other occasions where the maximum or minimum liquid height experience a sudden decrease can also be similarly explained. (k) The liquid rises through the pores between the particles and plates. (l) The liquid reaches the top surface of the particles at fourth row.

Figure 8 illustrates the snapshots of the rate-of-rise for nonuniform particle size wick case 3 at different simulation time steps. Figure 8(a) shows the particle arrangement between the parallel plates and the initial liquid height within the two plates at $t^* = 0$. (b) The liquid rises quickly to the top of the first particle row. (c) The high capillary pressure associated with the small pore between the plate and particles at the first and second row, i.e., Sp6 in Figure 4(c) provides a high capillary pressure that assist the liquid rise to the second row, i.e., $t^* = 32.98$. This is in contrast to the situation for case 2 at $t^* = 36.37$ where liquid rise to the second particle row took place mainly due to the small pore between the large particles in diagonal direction, i.e., Sp4 in Figure 4(b).

(d) Liquid detaches from the top surfaces of all the three particles in the first particle row relatively quickly at $t^* = 46.87$. Aside from the high capillary pressure associated with the small pores adjacent to the plate and in the diagonal direction, the relatively quick meniscus detachment from the top surface of the particles at the first particle row is due to the large permeable pore between the middle particles in the first and second row, i.e., Lp1 and Lp3 in Figure 4(b) and (c), respectively. (e) Liquid rise through the pores in the second particle row. The large pore between the particles in the second row, i.e., Lp4 in Figure 4(c) provide space for liquid to rise in the middle, i.e., $t^* = 72.92$. (f) The liquid that passes the small particles in the second row reaches the particles adjacent to the plate and rises sharply through the small pore between the plate and the particle in the third particle row. (g) The liquid rises to the top surface of the large particle at the third row quickly, and the small pore between the middle particles at the second and third particle row, i.e., Sp8 in Figure 4(c) provides a high capillary pressure by which the meniscus is detached from the top surface of the large middle particle much more quickly compared to the case 2. This is consistent with the shorter plateau of case 3 which ends much sooner than that of case 2 at $t^* = 130.2$ in the curve for the minimum liquid height in Figure 5(b). This interaction is visible in (g). (h) The small pore between the plate and the particles in the third and fourth particle row, i.e., Sp9 in Figure 4(c), provides a high capillary pressure by which the liquid reaches the small particle in the fourth row relatively quickly at $t^* = 152.8$. (i) The liquid detaches from the top surface of the particles in the third particle row and rise to the fourth particle row at $t^* = 225.7$. (h) The liquid reaches the top surface of the particles at the fourth row and continue to rise along the plate.

The minimum and maximum liquid heights do not always reflect the wickability. For example, in Figure 6(e), the maximum and minimum liquid heights show significant differences due to the

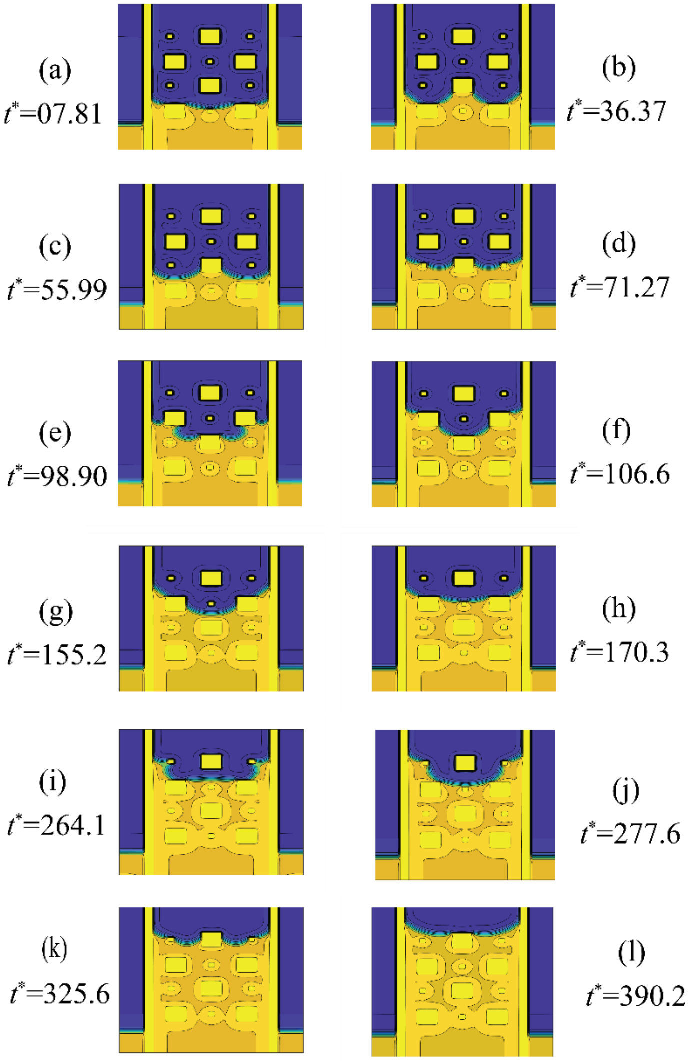

Figure 7: Snapshots of rate of rise in particle-filled parallel plates with nonuniform particle size wick case 2. The non-dimensional time-steps corresponding to each of the snapshots are also shown.

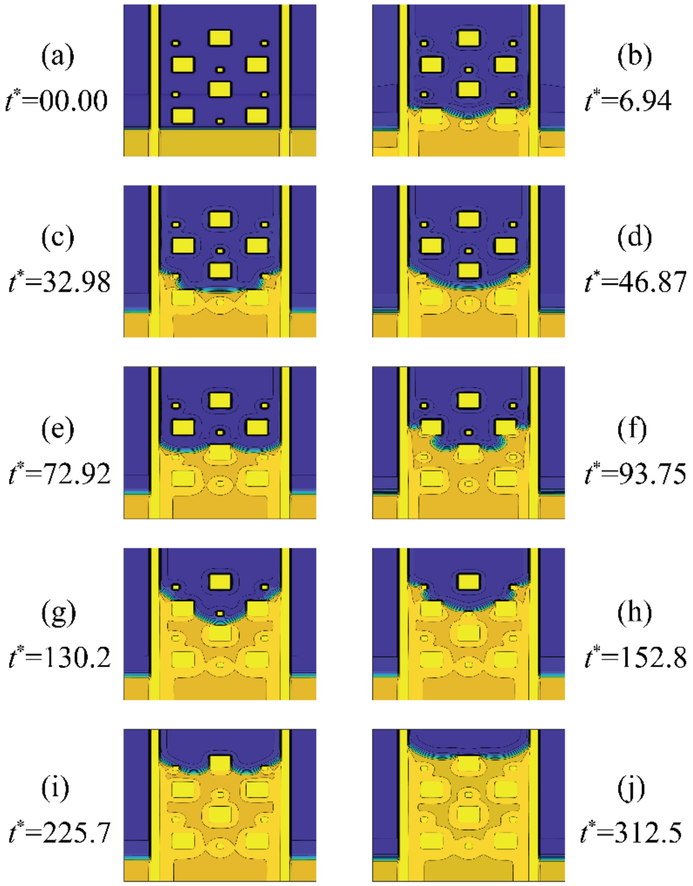

Figure 8: Snapshots of rate of rise in particle-filled parallel plates with nonuniform particle size distribution case 3. The non-dimensional time-steps corresponding to each of the snapshots are also shown.

different pore-scale capillary flow scenarios from the different capillary flow history and pore distributions. Thus, to simplify the capillary flow behaviors, dimensionless parameter η, liquid-filled pore ratio, which is the ratio between the pores filled with liquid to the maximum pore volume, η, i.e., liquid saturation, only within the space between the two plates.

Figure 9 shows the liquid-filled pore ratio, η, as a function of dimensionless time, t^*. This parameter is beneficial to characterize the liquid saturation in the pore structures. The uniform particle size wick (case 1) shows that the liquid filling is similar to those observed from the maximum and minimum liquid heights [see Figure 5(a) and (b)], i.e., step-wise pore filling. This is attributed to the fact that the capillary meniscus front advances by the capillary fingering through the pores formed between the two adjacent horizontal particles, while the liquid filling delays by the corner of the pores formed between the two adjacent vertical particles. While the same overall trend also applies to non-uniform particle size wicks, the period between the two sharp rises reduces compared to the uniform particle wick, due to the staggered capillary filling between the small and larger pores. While the higher η for case 3 compared to case 2 at $30 < t^* < 80$ is related to the enhanced capillary filling through the small pores between the particles and walls, i.e., Sp6 in Figure 4(c), the higher η at $t^* > 80$ is partly related to the small pore between the middle particle of row 2 and 3, i.e., Sp8 in Figure 4(c) and partly related to the small pore between the plate and the particles at the third and fourth rows, i.e., Sp9. The instantaneous enhancement of the liquid-filled pore ratio of the non-uniform particle size wick (case 2) is 68% compared to that of the uniform particle size wick (case 1) at $t^* = 148$ while it is about 75% in the non-uniform particle size wick (case 3) at $t^* = 148$. The cumulative (time integral) enhancement of the liquid-filled pore of the non-uniform particle size wick (case 2) is 12.31% compared to that of the uniform particle size wick (case 1), while it is 26.11% in the non-uniform particle size wick (case 3).

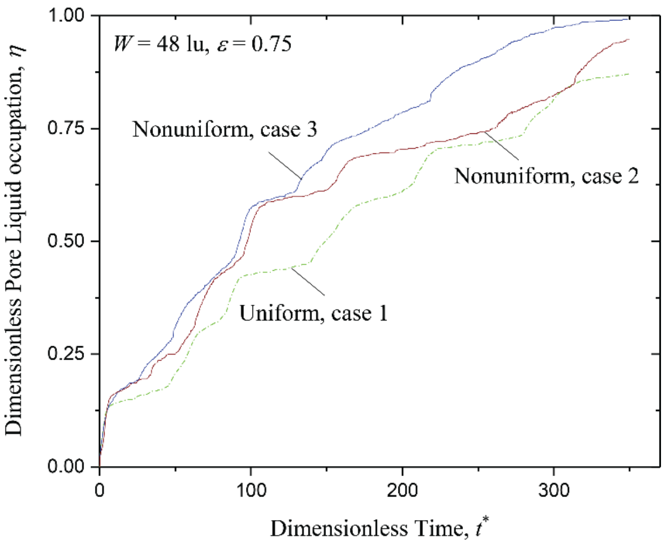

Figure 9: Dimensionless liquid filled pore ratio as a function of dimensionless time for uniform (case 1) and non-uniform particle size wicks (cases 2 and 3). The plate spacing W and porosity, ε, are also shown.

5. CONCLUSION

In this study, the free-energy-based, single-component, two-phase Lattice Boltzmann method (LBM) with a minimal parasitic current is utilized to predict the rate of rise through the capillary channels between the two parallel plates, uniform/non-uniform particle wicks between two plates. The LBM-predicted rate-of-rise between two parallel plates agrees well the analytical solution within RMS error of 10%. In the uniform particle size wick, the capillary meniscus front percolates though the pores by the periodic capillary filling, resulting in the step-wise rate-of-rise. The plateau periods increase as the liquid level increases. The LBM predicts that the non-uniform particle wick enhances the rate of rise by providing higher capillary pumping capability through the small pores and high permeability through the larger pores. The maximum and minimum liquid height and liquid-filled pore ratio are enhanced by 1.24%, 13.43%, and 12.31 for non-uniform particle size wick (case 2) and 11.1 %, 27.47%, and

26.11%, for non-uniform particle size wick (case 3), respectively. In practice, the non-uniform pore size distribution can be achieved by mixing the smaller and larger particles for the traditional furnace sintering process or by using 3D printing technique, which is currently being studied.

ACKNOWLEDGEMENTS

MB and GS are thankful for financial support by the National Science Foundation (NSF), Award No. OIA-1929187.

REFERENCES

[1] Liter, S. G., and Kaviany, M., 2001, “Pool-Boiling CHF Enhancement by Modulated Porous-Layer Coating: Theory and Experiment,” Int. J. Heat Mass Transf., **44**(22), pp. 4287–4311.

[2] Hwang, G. S., Nam, Y., Fleming, E., Dussinger, P., Ju, Y. S., and Kaviany, M., 2010, “Multi-Artery Heat Pipe Spreader: Experiment,” Int. J. Heat Mass Transf., **53**(13–14), pp. 2662–2669.

[3] Albu, N., Keese, J., and Hwang, G., 2019, “Bimodal, Thin Wick Structures for High Heat Flux Two-Phase Thermal Control Systems,” The 49th International Conference on Environmental Systems (ICES-2019-206), Boston, MA, USA.

[4] Egbo, M., Nasersharifi, Y., and Hwang, G., 2020, “Phase-Change Heat Transfer of Sintered-Particle Wick in Downward Facing Orientation: Particle Size and Wick Thickness Effects,” Int. J. Heat Mass Transf., **155**, p. 119840.

[5] Holley, B., and Faghri, A., 2006, “Permeability and Effective Pore Radius Measurements for Heat Pipe and Fuel Cell Applications,” Appl. Therm. Eng., **26**(4), pp. 448–462.

[6] Hoef, M. A. van der, Beetstra, R., and Kuipers, J. A. M., 2005, “Lattice-Boltzmann Simulations of Low-Reynolds-Number Flow Past Mono- and Bidisperse Arrays of Spheres: Results for the Permeability and Drag Force,” J. Fluid Mech. Camb., **528**, pp. 233–254.

[7] Nabovati, A., Llewellin, E. W., and Sousa, A. C. M., 2009, “A General Model for the Permeability of Fibrous Porous Media Based on Fluid Flow Simulations Using the Lattice Boltzmann Method,” Compos. Part Appl. Sci. Manuf., **40**(6), pp. 860–869.

[8] Liu, H., Valocchi, A. J., Kang, Q., and Werth, C., 2013, “Pore-Scale Simulations of Gas Displacing Liquid in a Homogeneous Pore Network Using the Lattice Boltzmann Method,” Transp. Porous Media, **99**(3), pp. 555–580.

[9] Faghri, A., 1995, *Heat Pipe Science And Technology*, Taylor & Francis.

[10] Feng, C., Yugeswaran, S., and Chandra, S., 2018, “Capillary Rise of Liquids in Thermally Sprayed Porous Copper Wicks,” Exp. Therm. Fluid Sci., **98**, pp. 206–216.

[11] He, X., Shan, X., and Doolen, G. D., 1998, “Discrete Boltzmann Equation Model for Nonideal Gases,” Phys. Rev. E, **57**(1), pp. R13–R16.

[12] Lee, T., and Fischer, P. F., 2006, “Eliminating Parasitic Currents in the Lattice Boltzmann Equation Method for Nonideal Gases,” Phys. Rev. E, **74**(4).

[13] Lee, T., and Liu, L., 2008, “Wall Boundary Conditions in the Lattice Boltzmann Equation Method for Nonideal Gases,” Phys. Rev. E, **78**(1), p. 017702.

[14] Connington, K., and Lee, T., 2013, “Lattice Boltzmann Simulations of Forced Wetting Transitions of Drops on Superhydrophobic Surfaces,” J. Comput. Phys., **250**, pp. 601–615.

[15] Wolf, F. G., Dos Santos, L. O., and Philippi, P. C., 2010, “Capillary Rise between Parallel Plates under Dynamic Conditions,” J. Colloid Interface Sci., **344**(1), pp. 171–179.

[16] Connington, K. W., Lee, T., and Morris, J. F., 2015, “Interaction of Fluid Interfaces with Immersed Solid Particles Using the Lattice Boltzmann Method for Liquid–Gas–Particle Systems,” J. Comput. Phys., **283**, pp. 453–477.